

## Nonpolar vertical GaN-on-GaN p–n diodes grown on free-standing (10 $\bar{1}$ 0) *m*-plane GaN substrates

Houqiang Fu<sup>1</sup>, Xiaodong Zhang<sup>2</sup>, Kai Fu<sup>1</sup>, Hanxiao Liu<sup>3</sup>, Shanthan R. Alugubelli<sup>3</sup>, Xuanqi Huang<sup>1</sup>, Hong Chen<sup>1</sup>, Izak Baranowski<sup>1</sup>, Tsung-Han Yang<sup>1</sup>, Ke Xu<sup>2,4</sup>, Fernando A. Ponce<sup>3</sup>, Baoshun Zhang<sup>2</sup>, and Yuji Zhao<sup>1\*</sup>

<sup>1</sup>School of Electrical, Computer, and Energy Engineering, Arizona State University, Tempe, AZ 85287, U.S.A.

<sup>2</sup>Key Laboratory of Nanodevices and Applications, Suzhou Institute of Nanotech and Nanobionics, CAS, Suzhou 215123, China

<sup>3</sup>Department of Physics, Arizona State University, Tempe, AZ 85287, U.S.A.

<sup>4</sup>Suzhou Nanowin Science and Technology Co., Ltd., Suzhou 215123, China

\*E-mail: yuji.zhao@asu.edu

Received August 17, 2018; accepted September 25, 2018; published online October 16, 2018

We report nonpolar vertical GaN-on-GaN p–n diodes grown on *m*-plane free-standing substrates. Cathodoluminescence measurements showed that the nonpolar p-GaN had a high quality with very few deep-level states. The device exhibited good rectifying behaviors with a turn-on voltage of 4.0 V, on-resistance of 2.3 m $\Omega$ ·cm<sup>2</sup>, and high on/off ratio of 10<sup>10</sup>. The reverse current leakage was described by a trap-assisted space-charge-limited current conduction mechanism. The critical electrical field was calculated to be 2.0 MV/cm without field plates or edge termination. These results pave the way for development of novel nonpolar power electronics and polarization-engineering-related advanced power devices.

© 2018 The Japan Society of Applied Physics

The wide-bandgap (WBG) semiconductor gallium nitride (GaN) has attracted considerable attention for efficient power conversion applications, owing to its WBG (3.4 eV), high breakdown electric field ( $\sim 3.0$  MV/cm), and high Baliga's figure of merit ( $\sim 10^3$  times higher than that of Si).<sup>1</sup> Owing to the lack of native GaN substrates, GaN-based power devices were usually heteroepitaxially grown on lattice-mismatched foreign substrates (e.g., sapphire) with large defect densities ( $>10^9$  cm<sup>-2</sup>), which limited the device performances.<sup>2,3</sup> Recently, the advancements in GaN crystal growth by hydride vapor phase epitaxy (HVPE) and ammonothermal method have provided commercially available free-standing bulk GaN substrates.<sup>4</sup> Homoepitaxial growths of GaN-based power devices on these substrates can enable significant reductions in defect densities and improvements in device performance.<sup>5,6</sup>

Owing to the availability of heavily doped GaN substrates, vertical power devices have been developed for high-voltage and high-power applications.<sup>1</sup> In contrast to lateral devices such as high-electron-mobility transistors (HEMTs),<sup>7</sup> in vertical devices, the currents flow vertically through the devices and the reverse voltages are held vertically. There are many advantages of the vertical structure over the lateral structure,<sup>1</sup> including a smaller chip area, larger current, lower sensitivity to surface states, better scalability, and smaller current dispersion, which is a big issue in HEMTs.<sup>7</sup>

Currently, the majority of vertical GaN-on-GaN power diodes such as p–n diodes<sup>5,6</sup> and transistors such as current-aperture vertical electron transistors (CAVETs)<sup>8</sup> and fin transistors<sup>9</sup> have been demonstrated on polar *c*-plane substrates [Fig. 1(a)]. The growth of devices along nonpolar crystal orientations [Fig. 1(b)] can provide unique material and device properties. The *m*-plane is significantly different from the *c*-plane in terms of atomic arrangement [Fig. 1(c)]. The *m*-plane consists of both Ga and N (1 : 1), while the *c*-plane is composed of only Ga.<sup>10</sup> Therefore, the polar GaN *c*-plane exhibits very strong spontaneous and piezoelectric polarization fields on the order of several MV/cm along the [0001] direction.<sup>11</sup> This led to various issues in GaN optoelectronics [e.g., light-emitting diodes (LEDs)], such as quantum confined Stark effect (QCSE)<sup>12</sup> and efficiency droop.<sup>4,13</sup>

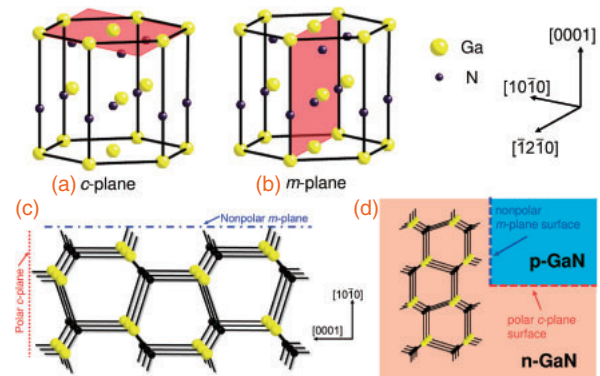


**Fig. 1.** (a) Polar *c*-plane and (b) nonpolar *m*-plane in the GaN wurtzite crystal unit cell. (c) Atomic arrangements of a *c*-plane and *m*-plane. (d) Schematic of selectively doped p–n junctions. During fabrications of VJFETs, JBS diodes, and SJs, the nonpolar surface is exposed, and a nonpolar p–n junction is formed.

The polarization-free nonpolar *m*-plane was then investigated to alleviate these issues.<sup>14</sup>

For power electronics, these polarization fields on the polar *c*-plane induce a high-density two-dimensional electron gas (2DEG) for lateral HEMTs, which are promising for high-frequency applications.<sup>1,7</sup> However, the 2DEG hinders the realization of a normally off device, which is desired for safe circuit operations. Nonpolar planes are advantageous for realization of normally off transistors with large threshold voltages.<sup>15,16</sup> Some advanced device concepts have been theorized on the nonpolar *m*-plane such as vertical-polarization-based superjunctions (SJs) and transistors.<sup>17,18</sup> In addition, there are increasing demands for more advanced GaN power device structures,<sup>19</sup> such as vertical junction field-effect transistors (VJFETs),<sup>20</sup> junction barrier Schottky (JBS) diodes, and SJs. The realization of these devices requires reliable selectively doped p–n junctions; in this regard, a proper understanding of nonpolar p–n junctions is crucial [Fig. 1(d)]. An approach to fabricate selectively doped p–n junctions is through ion implantation. However, the state-of-the-art hole concentration ( $N_A$ ) in the implanted p-GaN is only  $\sim 10^{16}$  cm<sup>-3</sup>.<sup>21</sup> On the other hand, an epitaxially grown p-GaN could achieve a significantly higher  $N_A$ , which makes

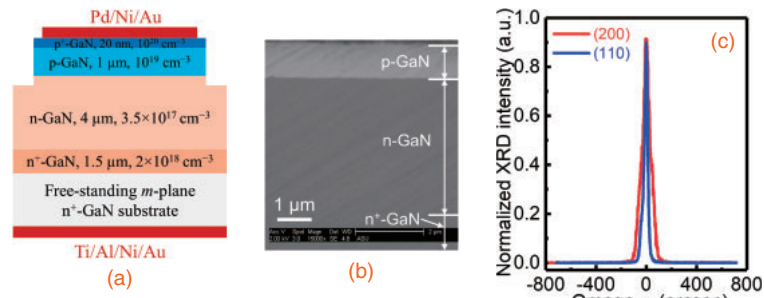


**Fig. 2.** (a) Schematic of the device structure of the nonpolar *m*-plane GaN p–n diode. (b) SEM image of the device cross-section. (c) (200)- and (110)-plane RCs of the device epilayer obtained by HRXRD.

the growth method more attractive for selectively doped p–n junctions. Despite these advantages and potential impacts, no extensive studies have been reported on growth of nonpolar power electronics; nonpolar vertical devices such as p–n diodes have not been demonstrated. Currently, compared with those with the nonpolar *a*-plane, nonpolar *m*-plane n<sup>+</sup>-GaN substrates are more easily available owing to their commercialization; *m*-plane epilayers with relatively good qualities can be obtained through growth optimizations.<sup>4)</sup> In this study, we perform comprehensive material and device characterizations of nonpolar vertical GaN-on-GaN p–n diodes grown on free-standing *m*-plane substrates. In addition, a following study on nonpolar *a*-plane diodes is ongoing. These results are valuable for the further development of advanced GaN power electronics such as VJFETs, JBS diodes, and SJs.

The epilayers of the nonpolar p–n diode were homoepitaxially grown on an *m*-plane n<sup>+</sup>-GaN free-standing substrate by metalorganic chemical vapor deposition (MOCVD). The growth temperature was 1050–1100 °C. Trimethylgallium (TMGa) and ammonia (NH<sub>3</sub>) were used as the source materials for Ga and N, respectively. Bis(cyclopentadienyl)magnesium (Cp<sub>2</sub>Mg) and silane (SiH<sub>4</sub>) were used as the precursors for p-type Mg dopants and n-type Si dopants, respectively. Hydrogen (H<sub>2</sub>) was used as the carrier gas to transport the reactants to the heated substrate in the MOCVD reactor. The V/III ratio was ~1800. Detailed information about the GaN growth by MOCVD can be found in Ref. 22. The device structure [Fig. 2(a)] consists of an n<sup>+</sup>-GaN buffer layer ([Si] =  $2 \times 10^{18} \text{ cm}^{-3}$ ), 4- $\mu\text{m}$ -thick n-GaN drift layer, p-GaN layer ([Mg] =  $10^{19} \text{ cm}^{-3}$ ), and p<sup>+</sup>-GaN contact layer ([Mg] =  $10^{20} \text{ cm}^{-3}$ ). Figure 2(b) shows an scanning electron microscopy (SEM) image of the device cross-section. The crystal quality of the epilayers was characterized by high resolution X-ray diffraction (HRXRD) using a PANalytical X'Pert Pro system. The X-ray source was the Cu K $\alpha$  radiation with a wavelength of 0.154 nm. The diffracted-beam optics was a triple axis module, and the incident-beam optics was a hybrid monochromator. Figure 2(c) shows the (200)- and (110)-plane rocking curves (RCs) of the sample. The full width at half maximum (FWHM) of the (200) RC was 39 arcsec, while that of the (110) RC was 30 arcsec. The dislocation density of the sample was estimated to be in the high  $10^6 \text{ cm}^{-2}$  range, according to Ref. 23.

The p-GaN layer of the nonpolar p–n diode was analyzed in detail by cathodoluminescence (CL) measurements, as p-doping in WBG semiconductors has been a challenging task; the p-GaN layer is crucial for the electrical properties of

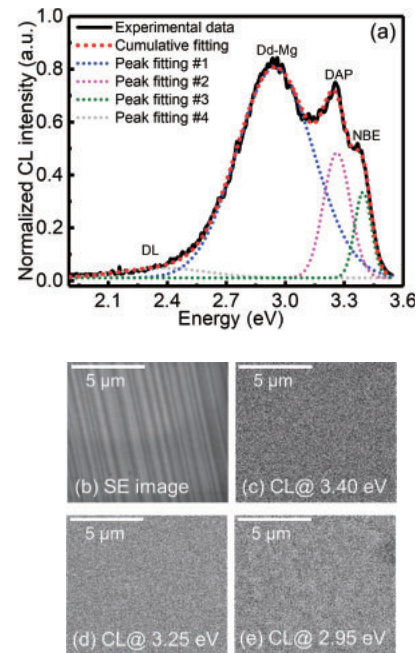


**Fig. 3.** (a) CL spectrum of the p-GaN layer of the nonpolar p–n diode. (b) SE image of the p-GaN layer. CL images of the p-GaN layer at (c) 3.40, (d) 3.25, and (e) 2.95 eV.

the GaN-based device. The CL spectrum was obtained using a JEOL 6300 SEM operating in the raster scan mode with an accelerating voltage of 7 kV and beam current of 100 pA at room temperature. CL images were recorded by setting the monochromator to a specific wavelength to study the spatial distribution of the CL intensity. In the CL spectrum in Fig. 3(a), several peaks are identified using Gaussian fitting. The peak at 3.40 eV is very close to the bandgap of GaN and is attributed to the free-exciton transition near the band edge, i.e., near-band-edge (NBE) transition.<sup>24)</sup> The peak at 3.25 eV is attributed to emissions of donor–acceptor pairs (DAPs) owing to conduction-band (CB)- or shallow-donor-to-Mg-acceptor transitions.<sup>25)</sup> The activation energy of Mg acceptors was estimated to be ~150 meV, calculated by the energy difference between the bandgap and DAP peak. The peak at 2.95 eV was assigned to a deep-donor (DD)-to-Mg-acceptor transition. This peak in p-GaN has been previously observed and attributed to nitrogen vacancies ( $V_N$ ).<sup>26)</sup> The formation of  $V_N$  is energetically favorable in p-GaN; most of the Mg acceptors are compensated by  $V_N$ , particularly at high Mg concentrations.<sup>26)</sup> Considering the self-compensation effect, we obtain that the net hole concentration in p-GaN is

$N_A \sim 10^{17} \text{ cm}^{-3}$ . In addition, we observed a very weak broad yellow-luminescence (YL) peak. This peak in GaN was well studied and assigned to a deep-level (DL) transition, i.e., CB-to-deep-acceptor (DA) transition.<sup>27)</sup> The weak DL transition indicated that the p-GaN layer on the nonpolar substrate had very few DAs. The SE image in Fig. 3(b) shows a striated morphology of the p-GaN layer with an undulated stripe-like surface, which is commonly observed in nonpolar and semipolar GaN, attributed to the in-plane diffusion anisotropy during the growth.<sup>4)</sup> Figures 3(c)–3(e) indicate that there was no noticeable spatial variation in the CL intensity, indicating a rather uniform p-GaN. These results showed that a high-quality p-GaN layer was obtained on the nonpolar substrate.

The nonpolar p–n diode was fabricated using the traditional optical photolithography, dry etching, and metal lift-off processes. First, the sample was cleaned in acetone and isopropyl alcohol solvents to remove organic contaminations and dipped in hydrochloric acid before metal depositions to remove native oxides on the surface. A mesa isolation of the device with a diameter of 230  $\mu\text{m}$  was then formed by a chlorine-based inductively coupled plasma (ICP) dry etching at an ICP power of 350 W, radio-frequency (RF) power of 70 W, and pressure of 5 mTorr with an etching depth of  $\sim 1 \mu\text{m}$ . Circular p-type ohmic contacts (diameter: 200  $\mu\text{m}$ ) were formed by Pd/Ni/Au metal stacks deposited by electron beam evaporation and subsequently annealed by rapid thermal annealing (RTA) at 450  $^\circ\text{C}$  for 5 min. For the n-type ohmic contact, nonalloyed Ti/Al/Ni/Au stacks were formed at the backside of the substrate using electron beam evaporation. It is worth noting that no passivation, field plate (FP), or edge termination were employed in the devices. On-chip electrical measurements were performed using a probe station. Capacitance–voltage ( $C$ – $V$ ) and forward current–voltage ( $I$ – $V$ ) characteristics were measured by a Keithley 4200-SCS parameter analyzer, and reverse  $I$ – $V$  characteristics were measured by a Keithley 2410 sourcemeter.

Figure 4(a) presents the forward  $I$ – $V$  characteristics of the nonpolar p–n diode in a linear scale. By extrapolating the leading edge of the  $I$ – $V$  curve to the  $x$ -axis, the turn-on voltage ( $V_{\text{on}}$ ) of the device was determined to be  $\sim 4.0 \text{ V}$ . The on-current of the device was limited by the upper current limit of the measurement setup (0.1 A) at 4.9 V, not intrinsically by the device. Light emissions from the device were also observed at high forward biases beyond  $V_{\text{on}}$ , owing to the radiative recombination of injected electrons and holes into the device. This usually indicates a good material quality of the epitaxial structure with a low defect density<sup>28)</sup> (confirmed by the HRXRD results), as defects can act as non-radiative recombination centers, quelling the light emission. A home-made electroluminescence (EL) setup using a charge-coupled device (CCD) spectrometer was used to analyze the emission spectrum. Three peaks were observed, at 367 (3.4 eV), 381 (3.25 eV), and 573 nm (2.2 eV). The first sharp peak was close to the bandgap of GaN, attributed to the NBE emission. The second peak at 3.25 eV was related to the DAP emission, as it was close to the energy difference from the CB to the Mg acceptor level. The third strong YL peak of GaN at 2.16 eV has been widely reported, related to the DL transition. Very few DAs were present in the p-GaN layer according to the CL analysis, suggesting that the majority of DAs in the device are located in the n-GaN drift layer. This is

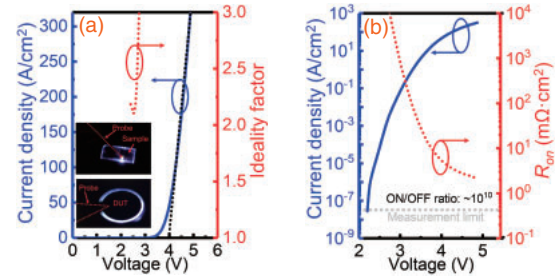


**Fig. 4.** (a) Forward  $I$ – $V$  and ideality factor as a function of the voltage in a linear scale. The inset shows the whole illuminated sample and device under test (DUT) at a high bias beyond  $V_{\text{on}}$ . (b) Current density and  $R_{\text{on}}$  as a function of the voltage in a semi-log scale.

consistent with first-principle calculations,<sup>29)</sup> which reveal that DAs are more likely to exist in n-GaN owing to the low formation energy. The origin of the DAs can be attributed to gallium vacancies ( $V_{\text{Ga}}$ ) or interstitial carbon ( $C_{\text{I}}$ ).<sup>30)</sup>

The ideality factor  $n$  of the device was obtained as a function of the voltage:

$$n = \frac{q}{2.3kT} \frac{1}{d \log J/dV}, \quad (1)$$

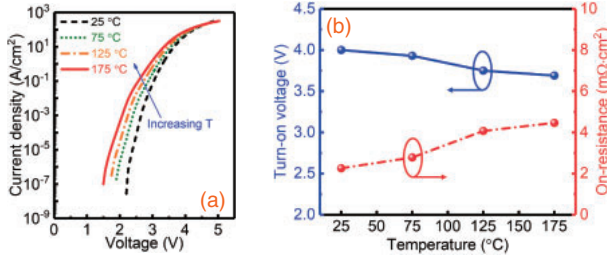
where  $q$  is the electron charge,  $k$  is the Boltzmann constant,  $T$  is the temperature, and  $J$  is the current density. At biases below 2.0 V, the current was below the setup detection limit, and  $n$  could not be obtained. The value of  $n$  initially decreased to a minimum at a certain voltage and then increased with the voltage, which is an expected behavior.<sup>31)</sup> The minimum  $n$  of the p–n diode was 2.1 at 2.50 V. Below 2.50 V, the transition from Shockley–Read–Hall (SRH) recombination current to diode diffusion current led to the decrease in  $n$ . The increase in  $n$  above 2.50 V originated from series resistance effects. Figure 4(b) shows the current density and on-resistance ( $R_{\text{on}}$ ) as a function of the voltage in a semi-log scale. The off-current density of the device was below  $10^{-7} \text{ A/cm}^2$ , limited by the apparatus lower current limit of 0.1 nA. The device exhibited a high on/off ratio on the order of  $\sim 10^{10}$ , which is among the highest values demonstrated in vertical GaN p–n diodes.<sup>5,11,28,32,33)</sup> At the current of 0.1 A (i.e., 0.3 kA/cm<sup>2</sup>), the device had an  $R_{\text{on}}$  of 2.3 m $\Omega$ ·cm<sup>2</sup>.

Figure 5(a) shows the temperature-dependent forward  $I$ – $V$  characteristics of the nonpolar p–n diode in the range of 25 to 175  $^\circ\text{C}$ .  $V_{\text{on}}$  and  $R_{\text{on}}$  were obtained as a function of the temperature, shown in Fig. 5(b).  $V_{\text{on}}$  decreased from 4.0 to 3.7 V, while  $R_{\text{on}}$  increased from 2.3 to 4.5 m $\Omega$ ·cm<sup>2</sup> with the increase in the temperature from 25 to 175  $^\circ\text{C}$ . The decrease in  $V_{\text{on}}$  with the increase in the temperature was attributed to the exponentially increasing diode diffusion current.<sup>31)</sup> A linear fitting of the experimental data showed that  $V_{\text{on}}$  decreased at a rate of 2.2 mV/ $^\circ\text{C}$ . The increase in  $R_{\text{on}}$  with the temperature was attributed to the reduced carrier mobility at a high temperature owing to the strong phonon scattering.<sup>6,34)</sup>

Figure 6 shows the  $C$ – $V$  and  $1/C^2$ – $V$  characteristics of the device at a frequency of 1 MHz. The net carrier concentration  $N_{\text{D}}$  of the drift layer of the diode can be obtained using

$$1/C^2 = \frac{2}{q\epsilon_0\epsilon_r N_{\text{D}}} (V_{\text{bi}} - V - 2kT/q), \quad (2)$$

$$\frac{d(1/C^2)}{dV} = -\frac{2}{q\epsilon_0\epsilon_r N_{\text{D}}}, \quad (3)$$



**Fig. 5.** (a) Temperature-dependent forward  $I$ - $V$  characteristics, from 25 to 175 °C. (b) Obtained  $V_{\text{on}}$  and  $R_{\text{on}}$  as a function of the temperature.

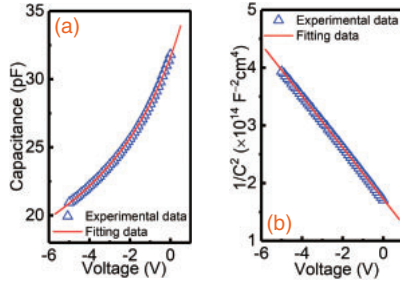


**Fig. 6.** (a)  $C$ - $V$  and (b)  $1/C^2$ - $V$  characteristics of the nonpolar p-n diode at 1 MHz.

where  $\epsilon_0$  is the permittivity of vacuum,  $\epsilon_r$  is the relative permittivity of GaN, and  $V_{\text{bi}}$  is the built-in voltage. The obtained  $N_D$  for the device drift layer was  $3.5 \times 10^{17} \text{ cm}^{-3}$ . Using the obtained  $N_D$ ,  $C$  and  $1/C^2$  curves were also calculated as a function of the voltage to compare them with the experimental data in Fig. 6; a good agreement between them was obtained.

Figure 7(a) presents the reverse  $I$ - $V$  characteristics of the nonpolar p-n diode in a log-log scale. A sudden change in the slope of the log  $I$ -log  $V$  curve of the device was observed at a hump voltage of  $V_{\text{TFL}}$  [trap-filled-limit (TFL) voltage] with a soft breakdown behavior.<sup>3,36</sup> When the reverse bias is below  $V_{\text{TFL}}$ , some of the injected electrons start to fill the DA traps, while the rest of them contribute to the reverse leakage current. At the reverse bias of  $V_{\text{TFL}}$ , the sudden increase in the slope of the logarithmic  $I$ - $V$  curve indicates that the electron-filling process of the DA traps is completed.<sup>32</sup> Such reverse characteristics can be described by an space-charge-limited-current (SCLC) conduction mechanism with traps:<sup>37,38</sup>

$$I = Aq^{1-l}\mu N_C \left[ \frac{\epsilon_0 \epsilon_r l}{N_T(l+1)} \right]^l \left( \frac{2l+1}{l+1} \right)^{l+1} \frac{V^{l+1}}{d^{2l+1}}, \quad (4)$$

where  $A$  is the device area,  $\mu$  is the mobility,  $N_C$  is the effective density of states,  $N_T$  is the trap density,  $d$  is the thickness, and  $l = E_{\text{CH}}/kT$ , where  $E_{\text{CH}}$  is the characteristic energy of the exponential tail states in the sub-bandgap region caused by traps. Therefore, in the SCLC transport,  $I$  is proportional to  $V^m$  where  $m = l + 1$ . A good linear fitting was obtained between  $\log I$  and  $\log V$  in the logarithmic  $I$ - $V$  curve of the device, where the coefficient of determination  $R^2$  was close to unity.  $m$  was 4.5; therefore,  $E_{\text{CH}}$  was 90.3 meV. Figure 7(b) shows the electric field profile of the device according to the one-dimensional Poisson's equation based on the punch-through model.<sup>39</sup> It should be noted that, according to the analysis, a non-punch-through model could not fit the experimental data.  $V_{\text{TFL}}$  was composed of electric potentials contributed by the ionized acceptors after the

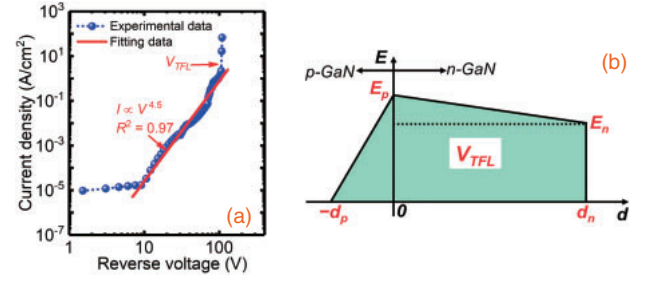


**Fig. 7.** (a) Reverse  $I$ - $V$  characteristics of the nonpolar p-n diode in a log-log scale. The data were fitted by the SCLC model. (b) Electric field profile along the growth direction of the device.

compensation effects, and ionized donors and charged DA traps in the p-GaN and n-GaN layers, respectively. Using the punch-through model, the electric field  $E_p$ ,  $E_n$ , and  $V_{\text{TFL}}$  can be expressed as

$$E_p = \frac{qN_A d_p}{\epsilon_0 \epsilon_r}, \quad (5)$$

$$E_n = E_p - \frac{q(N_D - N_T)d_n}{\epsilon_0 \epsilon_r}, \quad (6)$$

$$\begin{aligned} V_{\text{TFL}} &= \frac{1}{2} E_p d_p + \frac{1}{2} (E_p + E_n) d_n \\ &= \frac{qN_A d_p^2}{2\epsilon_0 \epsilon_r} + \frac{q[2N_A d_p - (N_D - N_T)d_n]d_n}{2\epsilon_0 \epsilon_r}, \end{aligned} \quad (7)$$

where  $d_p$  is the thickness of the p-GaN layer, while  $d_n$  is the thickness of the n-GaN layer. The nonpolar p-n diode had a  $V_{\text{TFL}}$  of 106 V;  $N_T$  was estimated to be  $3.0 \times 10^{17} \text{ cm}^{-3}$  according to Eq. (7). The critical electric field  $E_c$  is the larger value between  $E_p$  and  $E_n$ . After the calculation of  $E_p$  and  $E_n$  using Eqs. (5) and (6), respectively, and comparison, the obtained  $E_c$  for the device was 2.0 MV/cm, which is among the highest values reported for nonpolar power devices. It is also comparable to those of reported polar p-n diodes without FP or edge termination,<sup>11,23</sup> though it is still lower than the best value of polar devices ( $\sim 3.0$  MV/cm).  $E_c$  can be further improved by reducing the carrier concentration of the drift layer, adding passivation layers, and employing FPs and/or edge termination.

In summary, a nonpolar vertical GaN p-n diode was demonstrated on a free-standing  $m$ -plane GaN substrate by MOCVD. The material characterizations by HRXRD and CL indicated the good crystal quality of the  $m$ -plane epilayers with low defect densities and high-quality p-GaN with a significantly suppressed DL transition, which provided excellent electrical properties of the nonpolar p-n diode. The device had a  $V_{\text{on}}$  of 4.0 V,  $R_{\text{on}}$  of 2.3  $\text{m}\Omega\text{-cm}^2$ , high on/off ratio of  $10^{10}$ , and high  $E_c$  of 2.0 MV/cm. Owing to the fundamentally distinct polarization properties, nonpolar p-n junctions can not only provide an additional device design freedom for existing device structures such as HEMTs and CAVETs, but also can be incorporated into other advanced power electronic structures such as VJFETs, JBS diodes, and SJs. This study showed that high-performance nonpolar p-n diodes can be fabricated and easily used in various devices.

**Acknowledgments** This study was supported by the ARPA-E PNDI-ODES Program monitored by Dr. Isik Kizilyalli. We acknowledge the use of facilities within the Eyring Materials Center at the Arizona State University. Access to the NanoFab and/or EMC was supported, in part, by NSF award number NNCI-1542160.

- 1) S. Chowdhury and U. K. Mishra, *IEEE Trans. Electron Devices* **60**, 3060 (2013).
- 2) C. Gupta, Y. Enatsu, G. Gupta, S. Keller, and U. K. Mishra, *Phys. Status Solidi A* **213**, 878 (2016).
- 3) Y. Zhang, M. Sun, D. Piedra, M. Azize, X. Zhang, T. Fujishima, and T. Palacios, *IEEE Electron Device Lett.* **35**, 618 (2014).
- 4) Y. Zhao, H. Fu, G. T. Wang, and S. Nakamura, *Adv. Opt. Photonics* **10**, 246 (2018).
- 5) I. C. Kizilyalli, A. P. Edwards, H. Nie, D. Disney, and D. Bour, *IEEE Trans. Electron Devices* **60**, 3067 (2013).
- 6) H. Fu, X. Huang, H. Chen, Z. Lu, I. Baranowski, and Y. Zhao, *Appl. Phys. Lett.* **111**, 152102 (2017).
- 7) G. Meneghesso, G. Verzellesi, R. Pierobon, F. Rampazzo, A. Chini, U. K. Mishra, C. Canahi, and E. Zanoni, *IEEE Trans. Electron Devices* **51**, 1554 (2004).
- 8) D. Ji, M. A. Laurent, A. Agarwal, W. Li, S. Mandal, S. Keller, and S. Chowdhury, *IEEE Trans. Electron Devices* **64**, 805 (2017).
- 9) M. Sun, Y. Zhang, X. Gao, and T. Palacios, *IEEE Electron Device Lett.* **38**, 509 (2017).
- 10) S. C. Cruz, S. Keller, T. E. Mates, U. K. Mishra, and S. P. DenBaars, *J. Cryst. Growth* **311**, 3817 (2009).
- 11) Y. J. Cho, Z. Hu, K. Nomoto, H. Xing, and D. Jena, *Appl. Phys. Lett.* **110**, 253506 (2017).
- 12) V. Fiorentini, F. Bernardini, F. Della Sala, A. Di Carlo, and P. Lugli, *Phys. Rev. B* **60**, 8849 (1999).
- 13) H. Fu, Z. Lu, X. Zhao, Y. H. Zhang, S. P. DenBaars, S. Nakamura, and Y. Zhao, *J. Disp. Technol.* **12**, 736 (2016).
- 14) P. Waltereit, O. Brandt, A. Trampert, H. T. Grahn, J. Menniger, M. Ramsteiner, M. Reiche, and K. H. Ploog, *Nature* **406**, 865 (2000).
- 15) T. Fujiwara, S. Rajan, S. Keller, M. Higashiwaki, J. S. Speck, S. P. DenBaars, and U. K. Mishra, *Appl. Phys. Express* **2**, 011001 (2009).
- 16) M. Kuroda, H. Ishida, T. Ueda, and T. Tanaka, *J. Appl. Phys.* **102**, 093703 (2007).
- 17) H. Kawai, S. Yagi, S. Hirata, F. Nakamura, T. Saito, Y. Kamiyama, M. Yamamoto, H. Amano, V. Unni, and E. M. S. Narayanan, *Phys. Status Solidi A* **214**, 1600834 (2017).
- 18) V. Unni and E. M. S. Narayanan, *Jpn. J. Appl. Phys.* **56**, 04CG02 (2017).
- 19) H. Amano, Y. Baines, E. Beam, M. Borga, T. Bouchet, P. R. Chalker, M. Charles, K. J. Chen, N. Chowdhury, R. Chu, C. De Santi, M. M. De Souza, S. Decoutere, L. Di Cioccio, B. Eckardt, T. Egawa, P. Fay, J. J. Freedman, L. Guido, O. Häberlen, G. Haynes, T. Heckel, D. Hemakumara, P. Houston, J. Hu, M. Hua, Q. Huang, A. Huang, S. Jiang, H. Kawai, D. Kinzer, M. Kuball, A. Kumar, K. B. Lee, X. Li, D. Marcon, M. März, R. McCarthy, G. Meneghesso, M. Meneghini, E. Morvan, A. Nakajima, E. M. S. Narayanan, S. Oliver, T. Palacios, D. Piedra, M. Plissonnier, R. Reddy, M. Sun, I. Thayne, A. Torres, N. Trivellin, V. Unni, M. J. Uren, M. Van Hove, D. J. Wallis, J. Wang, J. Xie, S. Yagi, S. Yang, C. Youtsey, R. Yu, E. Zanoni, S. Zeltner, and Y. Zhang, *J. Phys. D* **51**, 163001 (2018).
- 20) D. Ji and S. Chowdhury, *IEEE Trans. Electron Devices* **62**, 2571 (2015).
- 21) Y. Zhang, Z. Liu, M. J. Tadjer, M. Sun, D. Piedra, C. Hatem, T. J. Anderson, L. E. Luna, A. Nath, A. D. Koehler, H. Okumura, J. Hu, X. Zhang, X. Gao, B. N. Feigelson, K. D. Hobart, and T. Palacios, *IEEE Electron Device Lett.* **38**, 1097 (2017).
- 22) S. Nakamura, G. Fasol, and S. J. Pearton, *The Blue Laser Diode: The Complete Story* (Springer, Heidelberg, 2000) 2nd ed.
- 23) H. Fu, X. Huang, H. Chen, Z. Lu, X. Zhang, and Y. Zhao, *IEEE Electron Device Lett.* **38**, 763 (2017).
- 24) L. H. Robins, K. A. Bertness, J. M. Barker, N. A. Sanford, and J. B. Schlager, *J. Appl. Phys.* **101**, 113506 (2007).
- 25) A. M. Fischer, S. Wang, F. A. Ponce, B. P. Gunning, C. A. M. Fabien, and W. A. Doolittle, *Phys. Status Solidi B* **254**, 1600668 (2017).
- 26) S.-W. Kim, J.-M. Lee, C. Huh, N.-M. Park, H.-S. Kim, I.-H. Lee, and S.-J. Park, *Appl. Phys. Lett.* **76**, 3079 (2000).
- 27) I. Shalish, L. Kronik, G. Segal, Y. Rosenwaks, Y. Shapira, U. Tisch, and J. Salzman, *Phys. Rev. B* **59**, 9748 (1999).
- 28) M. Qi, K. Nomoto, M. Zhu, Z. Hu, Y. Zhao, V. Protasenko, B. Song, X. Yan, G. Li, J. Verma, S. Bader, P. Fay, H. Xing, and D. Jena, *Appl. Phys. Lett.* **107**, 232101 (2015).
- 29) J. Neugebauer and C. G. Van de Walle, *Appl. Phys. Lett.* **69**, 503 (1996).
- 30) Y. Saitoh, K. Sumiyoshi, M. Okada, T. Horii, T. Miyazaki, H. Shiomi, M. Ueno, K. Katayama, M. Kiyama, and T. Nakamura, *Appl. Phys. Express* **3**, 081001 (2010).
- 31) K. Nomoto, B. Song, Z. Hu, M. Zhu, M. Qi, N. Kaneda, T. Mishima, T. Nakamura, D. Jena, and H. G. Xing, *IEEE Electron Device Lett.* **37**, 161 (2016).
- 32) H. Fu, K. Fu, X. Huang, H. Chen, I. Baranowski, T.-H. Yang, J. Montes, and Y. Zhao, *IEEE Electron Device Lett.* **39**, 1018 (2018).
- 33) Y. Zhang, M. Yuan, N. Chowdhury, K. Cheng, and T. Palacios, *IEEE Electron Device Lett.* **39**, 715 (2018).
- 34) Z. H. Liu, S. Arulkumar, and G. I. Ng, *Appl. Phys. Lett.* **94**, 142105 (2009).
- 35) H. Fu, I. Baranowski, X. Huang, H. Chen, Z. Lu, J. Montes, X. Zhang, and Y. Zhao, *IEEE Electron Device Lett.* **38**, 1286 (2017).
- 36) C. Zhou, Q. Jiang, S. Huang, and K. J. Chen, *IEEE Electron Device Lett.* **33**, 1132 (2012).
- 37) J. A. Röhr, D. Moia, S. A. Haque, T. Kirchartz, and J. Nelson, *J. Phys.: Condens. Matter* **30**, 105901 (2018).
- 38) Y. Son and R. L. Peterson, *Semicond. Sci. Technol.* **32**, 12LT02 (2017).
- 39) Y. Zhang, A. Dadgar, and T. Palacios, *J. Phys. D* **51**, 273001 (2018).